

## *In situ* XRD investigation of the evolution of surface layers on Pb-alloy anodes

Marie Clancy,<sup>1</sup> Mark J. Styles,<sup>2</sup> Colleen J. Bettles,<sup>1</sup> Nick Birbilis,<sup>1</sup> Justin A. Kimpton,<sup>3</sup> and Nathan A. S. Webster<sup>4,a)</sup>

<sup>1</sup>Department of Materials Science and Engineering, Monash University, Clayton, VIC 3800, Australia

<sup>2</sup>CSIRO Manufacturing, Private Bag 10, Clayton, VIC 3169, Australia

<sup>3</sup>Australian Synchrotron, 800 Blackburn Rd, Clayton, VIC 3168, Australia

<sup>4</sup>CSIRO Mineral Resources, Private Bag 10, Clayton South, VIC 3169, Australia

(Received 6 March 2017; accepted 23 May 2017)

The electrochemical behaviour of a number of Pb-based anode alloys, under simulated electrowinning conditions, in a 1.6 M H<sub>2</sub>SO<sub>4</sub> electrolyte at 45 °C was studied. Namely, the evolution of PbO<sub>2</sub> and PbSO<sub>4</sub> surface layers was investigated by quantitative *in situ* synchrotron X-ray diffraction (S-XRD) and subsequent Rietveld-based quantitative phase analysis (QPA). In the context of seeking new anode alloys, this research shows that the industry standard Pb-0.08Ca-1.52Sn (wt%) anode, when exposed to a galvanostatic current and intermittent power interruptions, exhibited poor electrochemical performance relative to select custom Pb-based binary alloys; Pb-0.73Mg, Pb-5.05Ag, Pb-0.07Rh, and Pb-1.4Zn (wt%). The *in situ* S-XRD measurements and subsequent QPA indicated that this was linked to a lower proportion of β-PbO<sub>2</sub>, relative to PbSO<sub>4</sub>, on the Pb-0.08Ca-1.52Sn alloy at all stages of the electrochemical cycling. The best performing alloy, in terms of minimisation of overpotential during normal electrowinning operation and minimising the deleterious effects of repeated power interruptions – both of which are significant factors in energy consumption – was determined to be Pb-0.07Rh. © 2017 International Centre for Diffraction Data. [doi:10.1017/S0885715617000793]

Key words: copper electrowinning, power interruption, PbO<sub>2</sub> and PbSO<sub>4</sub> surface layers, *in situ* synchrotron X-ray diffraction, quantitative phase analysis

### I. INTRODUCTION

In an industrial electrowinning tank-house used for the solvent extraction of copper (Cu), lead (Pb)-based alloy anodes are placed in a bath of concentrated sulphuric acid in an alternating sequence with stainless steel cathodes (Schlesinger *et al.*, 2011). Under galvanostatic (constant current) conditions, the Cu dissolved in the acid electrolyte is plated on to the cathode while O<sub>2</sub> is evolved at the anode, because of the significant anodic polarisation on the anode being in the oxygen evolution regime (i.e. >1 V<sub>NHE</sub>). To harvest a sheet of Cu takes about 7 days, but the Pb-based anodes are expected to have an average lifetime of about 5 years (Camurri *et al.*, 2001). The lifetime of the Pb-based anode is strongly influenced by the behaviour of the passivating layer that forms on its surface, which evolves from PbSO<sub>4</sub> to PbO<sub>2</sub> depending on the pH of the electrolyte and the potential applied to the anode.

Given rising energy costs worldwide and concerns about greenhouse gas emissions, there exists a need to design anodes that can help to reduce the amount of energy consumed during solvent extraction processes, including electrowinning. Any given tank-house can contain thousands of Pb-alloy anodes in acid baths, and therefore a small percentage reduction in

energy consumption could translate to millions of dollars being saved annually, with significant emission reductions. In industrial electrowinning, a power interruption in the cell can occur for a number of reasons, leaving the Pb-based anodes exposed at their open-circuit potential (OCP) while immersed in the H<sub>2</sub>SO<sub>4</sub> electrolyte, and allowing potentially unfavourable chemical reactions such as the transformation of PbO<sub>2</sub> back to PbSO<sub>4</sub> to occur. This scenario is comparable with the charge/discharge (ON-OFF) situation in a lead acid battery (Pavlov and Monahov, 1996). In electrowinning applications, a PbO<sub>2</sub> surface layer is more desirable than PbSO<sub>4</sub>, as PbO<sub>2</sub> is often present as a dense, compact and (electron) conductive film (Pavlov, 2011), properties which are all critical to the efficiency of the Cu electrowinning process.

At present, the commonly used Pb-based anode in industry has a composition of Pb-0.08Ca-1.52Sn (wt%). In the present work, the effects of different alloying elements on the electrochemical performance of Pb-based anode alloys when exposed to alternating galvanostatic (GALV) and power interruption (open circuit) conditions are investigated. Each of the compositions investigated was selected based on preliminary testing on the basis that they exhibited an apparently superior performance relative to the industry standard alloy. This follows on from our recent *in situ* synchrotron X-ray diffraction (S-XRD) investigation of PbO<sub>2</sub>/PbSO<sub>4</sub> surface layer evolution during electrochemical cycling of a pure Pb anode (Clancy *et al.*, 2015), where it was shown for the first time that it is

<sup>a)</sup> Author to whom correspondence should be addressed. Electronic mail: [nathan.webster@csiro.au](mailto:nathan.webster@csiro.au)

possible to characterise the PbO<sub>2</sub>/PbSO<sub>4</sub> surface layer evolution, both in terms of the relative weight fractions of the crystalline phases and the layer thickness, in a sulphuric acid electrolyte and in real time. An *in situ* approach to surface layer characterisation is superior to an *ex situ* one since the anode remains in the cell with electrolyte flowing over the anode surface, and avoids artefacts introduced by the extraction of the sample from its operational conditions.

## II. EXPERIMENTAL

### A. Alloy compositions and preparation

Four Pb-based alloys were investigated in addition to 99.97% pure Pb and the industry standard alloy used in copper electrowinning (Pb–0.08Ca–1.52Sn); the custom Pb-binary alloys studied were Pb–0.73Mg, Pb–0.05Ag, Pb–0.07Rh, and Pb–1.4Zn. All alloy compositions are given in wt%. For the purpose of this investigation all alloys were studied in their as-cast form, including the industry standard Pb–Ca–Sn. The compositions selected were close to the maximum of solubility of each dopant in pure Pb (and hence the unique alloy loading in each case). The custom alloys were produced *via* the conventional crucible method. Finely chopped pieces of Pb and powdered alloying elements were heated in a quartz tube that was backfilled with argon (Ar) before sealing. The quartz tube was placed in a muffle furnace and held for extended periods at temperatures suitable for alloying of the respective elements. The alloy compositions were externally confirmed by ICP-AES (Spectrometer Services, Coburg, Australia). To enable the *in situ* S-XRD experimentation using a novel electrochemical flow cell [such a cell was previously described in Clancy *et al.* (2015)] a section of each alloy was mounted in epoxy resin before the surfaces were ground to a 1200 grit finish using SiC paper.

### B. *In situ* S-XRD

*In situ* S-XRD experiments were performed on the powder diffraction beamline at the Australian Synchrotron. Schematics of the flow cell and photographs of the experimental setup have been provided previously (Clancy *et al.*, 2015). 1.6 M H<sub>2</sub>SO<sub>4</sub> (sulphuric acid) solution was pumped over the alloy at 45 °C, and S-XRD data were collected throughout six galvanostatic – open circuit (GALV-OCP) electrochemical cycles, with individual data sets collected for 1 min using two detector positions, *P1* and *P2* (the detector contains 0.2° gaps every 5°2θ; data were collected in two detector positions 0.5° apart in order to cover the entire 2θ range). Asymmetric diffraction geometry with an incident beam-to-sample angle (defined hereafter as ω) of 8° was utilised for data collection, over the range 10° ≤ 2θ ≤ 90°. The vertical and horizontal slit widths were 0.2 and 5.0 mm, respectively. The X-ray wavelength was 0.9998 Å and was calibrated using LaB<sub>6</sub> (NIST 660b line position standard) contained in a 0.3 mm diameter glass capillary.

For the purposes of visualisation of the formation and decomposition of phases as the electrochemical experiment progressed, individual *P1* and *P2* data sets were merged using CONVAS2 (Rowles, 2010) to remove the detector gaps. Merged data sets were stacked to produce a plot of accumulated data with elapsed time plotted vs. 2θ, viewed down

the intensity axis. The merged data sets were also used for Rietveld refinement-based quantitative phase analysis (QPA) implemented in TOPAS (Bruker, 2014). A correction to account for sample displacement error in the asymmetric diffraction geometry was incorporated into the refinement model, as was an intensity correction to account for the asymmetric diffraction geometry and also the absorption of the diffracted X-rays in H<sub>2</sub>SO<sub>4</sub>. Details of the models have been provided previously (Clancy *et al.*, 2015). Phase concentration values are relative crystalline wt% calculated *via* the Hill and Howard (1987) algorithm. The crystal structure information reported in Goodwin and Whetstone (1947), Straumanis (1949), Wyckoff (1963) and D'Antonio and Santoro (1980) were used for Pb, β-PbO<sub>2</sub>, α-PbO<sub>2</sub>, and PbSO<sub>4</sub>, respectively. An anisotropic crystallite size broadening correction was implemented to account for the observed peak profiles for the β-PbO<sub>2</sub> phase, to improve the quality of fit of the profile calculated using the conventional crystallite size (CS) and microstrain (MS) models. Details of the model, including equations, have been provided previously (Clancy *et al.*, 2015), with Lorentzian CS and MS being refineable parameters in the Rietveld analysis.

For the purposes of calculation of the thickness (*t*) of the PbO<sub>2</sub>/PbSO<sub>4</sub> surface layer as a function of time, the decay in intensity (*I*/*I*<sub>0</sub>) of the (111) Pb reflection at 20.2°2θ was implemented in (Cullity, 1978).

$$\frac{I}{I_0} = e^{-\mu t(1/\sin \omega + 1/\sin \beta)} \quad (1)$$

where μ is the X-ray linear absorption coefficient of the PbO<sub>2</sub>/PbSO<sub>4</sub> surface layer, ω is 8° and β is the angle of the diffracted beam to the detector (i.e. β = 2θ – ω = 12.2° for the (111) Pb reflection). The relative concentrations of β-PbO<sub>2</sub>, α-PbO<sub>2</sub>, and PbSO<sub>4</sub> returned from the QPA were used to calculate the value of μ at each data point. This approach assumes crystallographic density of the surface layers, and is treated as a semi-quantitative approach only without accurate knowledge of the actual surface layer density as a function of time.

### C. Electrochemical conditions

The working electrode (Pb-based anode alloy) was exposed to a galvanostatic signal *via* a BioLogic® SP-150 potentiostat in conjunction with EC-Lab software. The potentiostat was connected to the cell *via* leads to the working electrode, the Ag/AgCl reference electrode and a Pt counter electrode. The applied current was equal to that used in industrial tank-houses, such that the current density was 300 A m<sup>-2</sup> for each sample. After 40 min of applied galvanostatic current, the OCP was recorded for a 30 min period, during which no applied current was imposed to the system. This experiment was designed to examine the performance of the Pb-based anodes during a tank-house power failure or when the power is switched off. The galvanostatic segment, followed by the OCP segment, which made up one cycle, was repeated a further five times to record the evolution of the electrochemical performance of the Pb-based anode. It is important to note that the reference electrode used for the *in situ* flow cell study utilised an Ag/AgCl electrode, which has a potential difference of +0.199 V versus the standard hydrogen electrode.

### III. RESULTS AND DISCUSSION

#### A. Electrochemical characteristics of Pb-alloys

The electrochemical potential versus time plots during the galvanostatic–OCP cycling for (a) Pb–Mg, (b) Pb–Ag, (c) Pb–Rh, (d) Pb–Zn, and (e) pure Pb alloys, are individually compared against the Pb–Ca–Sn alloy (Figure 1). There was a minor disturbance caused by a bubble in the cell for the Pb–Rh alloy. This is evidenced in Figure 1(c) by a spike in the measured potential in the first cycle, but was resolved once the bubble migrated away from the surface of the working electrode surface. During the OCP segments the PbO<sub>2</sub> transforms to PbSO<sub>4</sub> at a potential of  $\sim 1.25$  V<sub>Ag/AgCl</sub>. The rate at which each system undergoes the PbO<sub>2</sub> to PbSO<sub>4</sub> transformation, and to what extent over the 30 min period, varies significantly as can be seen in the results presented in Figure 4.

The systems ranked in descending rate of transformation, were Pb–Ca–Sn, Pb, Pb–Zn, Pb–Mg, Pb–Ag, and Pb–Rh. In other words, the “best” performing alloy overall was considered to be the Pb–Rh alloy, with the Pb–Ag alloy only marginally behind in performance. Such an assessment is also based on the lower overpotential ( $\sim 1.5$  V<sub>Ag/AgCl</sub>) achieved in response to the same galvanostatic polarisation conditions as the Pb–Ca–Sn, Pb–Mg, Pb–Zn, and pure Pb alloys (each measuring an overpotential of  $\sim 1.7$  V<sub>Ag/AgCl</sub>). This can have a significant (beneficial) effect in lowering the overall energy requirement of the cell, where the power requirement is  $i \times V$ , where “ $i$ ” is a constant fixed galvanostatic current, and “ $V$ ” (in the context of power requirement) is the overpotential. Herein, the overpotential resulting from Rh and Ag additions

is minimised, translating to a lower overall power requirement. Furthermore, the reduced change in the OCP across the six cycles compared with the other alloys is also unique to the Pb–Rh alloy. For example, the potential during the OCP segment of the first cycle for the Pb–Rh alloy reached a minimum value of 0.14 and 0.25 V<sub>Ag/AgCl</sub> in the sixth cycle. In comparison, the potential during the OCP segment of the first cycle for the Pb–Ca–Sn alloy reached a minimum value of 0.21, and 0.98 V<sub>Ag/AgCl</sub> in the sixth cycle. Based on these measures, the Pb–Mg, and Pb–Zn anodes also exhibit improved electrochemical performance from electrochemical testing, when compared with Pb–Ca–Sn. The stark differences induced by relatively low level alloying additions are indeed significant. It should be noted, however, that properties such as good mechanical strength and creep resistance, which are key factors in pure Pb being an unsuitable anode material for industrial use, must also be taken into account when considering an alloy to replace the industry standard. One feature of the Pb–Rh, and Pb–Ag alloys identified here, however, and which is a factor that would require longer term testing, is the minor increase in potential with each galvanostatic cycle, compared with the insignificant change in the potential galvanostatic region for the other alloys.

#### B. Surface evolution and phase analysis

Figure 2 reveals the plot of accumulated *in situ* S-XRD data for the Pb–Mg alloy. The first of the six galvanostatic and OCP segments is labelled. During the galvanostatic

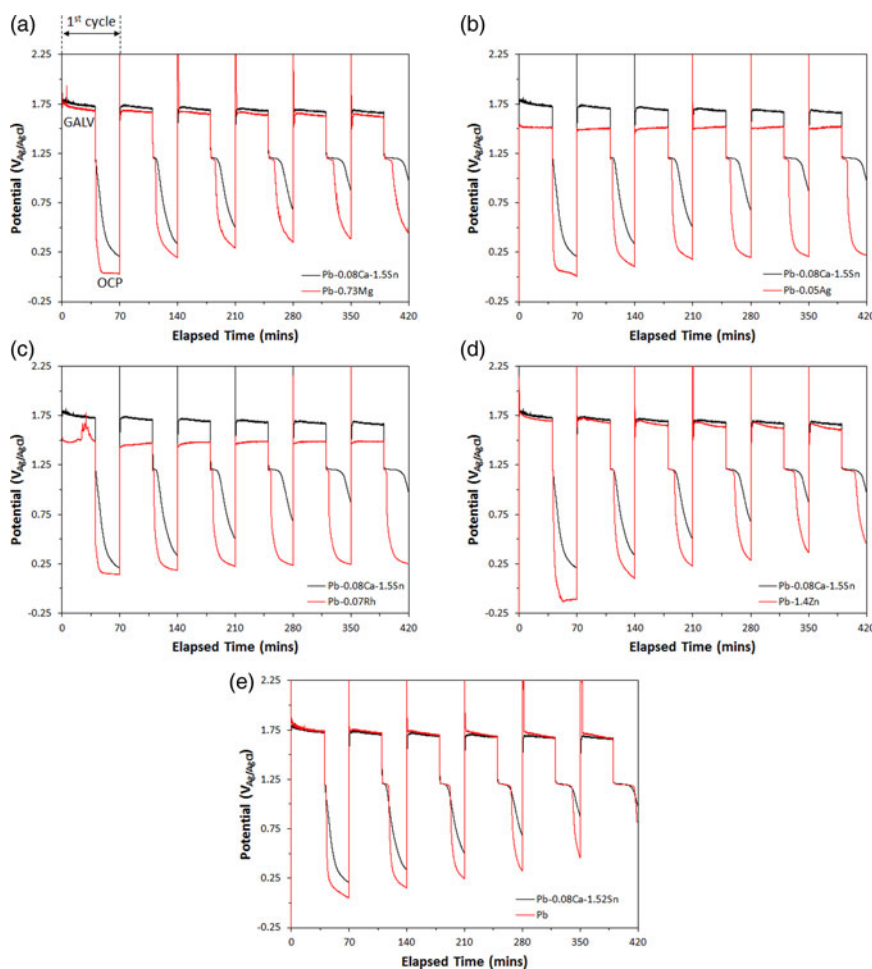


Figure 1. (Colour online) Potential versus time plots for the (a) Pb–0.73Mg, (b) Pb–0.05Ag, (c) Pb–0.07Rh, and (d) Pb–1.4Zn alloys (red traces), compared with the industry standard Pb–0.08Ca–1.52Sn alloy (black trace). For completeness the results reported by Clancy *et al.* (2015) for the pure Pb anode are also shown in (e). The GALV and OCP segments of the first electrochemical cycle for the Pb–Mg/Pb–Ca–Sn alloys are labelled in (a).

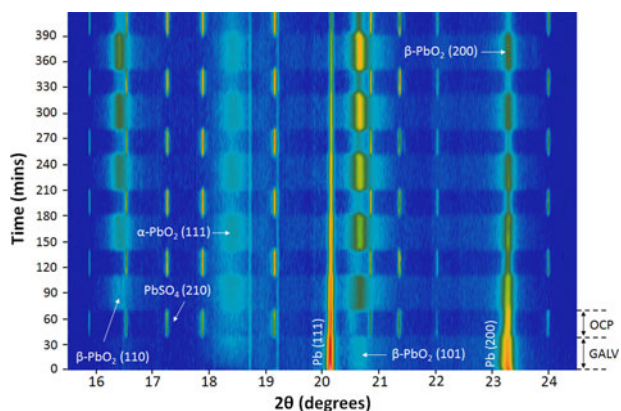


Figure 2. (Colour online) A plot of accumulated diffraction data collected for the Pb-0.73Mg alloy during electrochemical cycling, where GALV = galvanostatic and OCP = power interruption regimes. Some of the key Pb,  $\beta$ -PbO<sub>2</sub>,  $\alpha$ -PbO<sub>2</sub>, and PbSO<sub>4</sub> reflections are labelled. The features at  $\sim 18.7^\circ$  and  $19.2^\circ 2\theta$ , which are present over the duration of the experiment are artefacts from the detector.

segments, the tetragonal  $\beta$  and orthorhombic  $\alpha$  polymorphs of PbO<sub>2</sub> both formed, while the orthorhombic form of PbSO<sub>4</sub> formed during the OCP segments. Other than those from the substrate, no reflections from any other phases were observed during the experiment.  $\alpha$ -PbO<sub>2</sub> was observed together with the  $\beta$  phase during the galvanostatic segments of the experiments performed for the Pb–Ca–Sn, Pb–Ag, and Pb–Zn alloys; for pure Pb and the Pb–Rh alloy however,  $\beta$ -PbO<sub>2</sub> was the only phase observed during the galvanostatic segments. A shift of the broad PbO<sub>2</sub> reflections to lower  $2\theta$  during conversion of this phase to PbSO<sub>4</sub> was observed, which is attributed to substitution of larger Pb<sup>2+</sup> (ionic radius = 1.33 Å) (Shannon, 1976) cations for Pb<sup>4+</sup> (0.915 Å) in the  $\beta$ -PbO<sub>2</sub> structure during conversion to PbSO<sub>4</sub>, forming a non-stoichiometric phase (Butler and Copp, 1956).

Another noteworthy feature of the *in situ* S-XRD data is that the  $\beta$ -PbO<sub>2</sub> peaks for Pb–Rh, and Pb–Ag (seen specifically for Pb–Ag in Figure 3) are significantly sharper than those observed in the data for the other alloys investigated. This manifests in a higher value for the CS parameter in our anisotropic CS broadening model (Table I). Owing to the

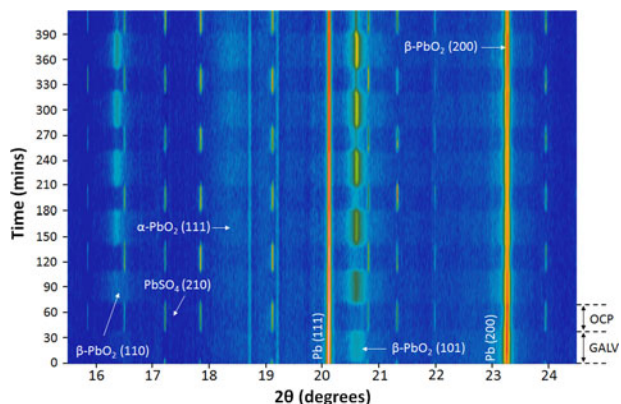


Figure 3. (Colour online) A plot of accumulated diffraction data collected for the Pb-0.05Ag alloy during electrochemical cycling. The  $\beta$ -PbO<sub>2</sub> peaks are significantly narrower in these data, compared with the Pb-0.73Mg sample (Figure 2), indicating a larger average crystallite size.

TABLE I. Refined values of the Lorentzian crystallite size (CS, in nm) and micro-strain (MS) parameters for  $\beta$ -PbO<sub>2</sub> in the dataset collected after 237 min i.e. during the fourth galvanostatic segment) for each alloy. The numbers in parentheses are Rietveld errors indicative of error in fit between the experimental and calculated profiles.

Alloy	CS	MS
Pb–Ca–Sn	32.2(0.1)	0.7(0.1)
Pb–Mg	32.0(0.1)	0.5(0.1)
Pb–Ag	135.4(0.2)	0.4(0.1)
Pb–Rh	97.0(0.2)	0.4(0.1)
Pb–Zn	22.9(0.1)	0.3(0.1)
Pb	48.3(0.1)	0.5(0.1)

nature of the experimental setup and the assumptions in the modelling employed, these values are only an approximate measure of the CS. However, they can provide a qualitative insight into the microstructure of the  $\beta$ -PbO<sub>2</sub> layer on the different alloys, namely the  $\beta$ -PbO<sub>2</sub> crystallites appear larger on the Pb–Ag and Pb–Rh than on the other alloys. The CS value for the Pb–Ag alloy was higher than that for Pb–Rh, which may be the property giving rise to the greater upwards slope of the galvanostatic segment for this alloy, thought to be a potential indicator of a lack of long term stability in the oxide layer.

### C. QPA and thickness evolution

The comprehensive results of Rietveld refinement-based QPA are presented in Figure 4, showing the evolution in relative concentration of the alloy substrate and the  $\beta$ -PbO<sub>2</sub>,  $\alpha$ -PbO<sub>2</sub>, and PbSO<sub>4</sub> surface layers as a function of time. It should be noted that the S-XRD data collection for the Pb–Zn alloy stopped after 248 min because of an unforeseen loss of the X-ray beam, whereas the electrochemistry was allowed to continue until after the sixth cycle was complete. Figure 4(b) shows the QPA results for the Pb–Mg alloy, and general trends observed across Figures 4(a)–4(e) are discussed in relation to these results. Both  $\beta$ - and  $\alpha$ -PbO<sub>2</sub> formed immediately on the substrate, and continued to grow during the galvanostatic segment of the first cycle, as indicated by the increase in crystalline phase concentration from 6 wt% ( $\beta$ -PbO<sub>2</sub>) and 2 wt% ( $\alpha$ -PbO<sub>2</sub>) at  $t=0$  min, to 22 and 9 wt%, respectively at the end of the segment ( $t=38$  min). The concentration of  $\beta$ -PbO<sub>2</sub> also increased as the number of cycles increased;  $\beta$ -PbO<sub>2</sub> represented 45 wt% at the start of the galvanostatic segment of the second cycle ( $t=74$  min), compared with 22 wt% at the end of the galvanostatic segment of the first cycle, for example. In addition, whilst at each of the OCP to galvanostatic transitions the PbSO<sub>4</sub> transforms completely, the dissolution of  $\beta$ - and  $\alpha$ -PbO<sub>2</sub> at the galvanostatic to OCP transitions is incomplete and the amount of residual PbO<sub>2</sub> increases, reaching 25 wt% (for  $\beta$ -PbO<sub>2</sub>) in the final cycle. No  $\alpha$ -PbO<sub>2</sub> was detected on the Pb and Pb–Rh surfaces during cycling, whereas the Pb–Mg and Pb–Zn systems showed the most significant amounts which remained quite stable throughout electrochemical exposure. After the six galvanostatic cycles the Pb–Ca–Sn, Pb–Mg, Pb–Zn, and Pb alloys all had combined relative phase concentrations of  $\beta$ -PbO<sub>2</sub> and PbSO<sub>4</sub> that were significantly higher than those of the Pb–Ag and Pb–Rh alloys. Given that the detected Pb

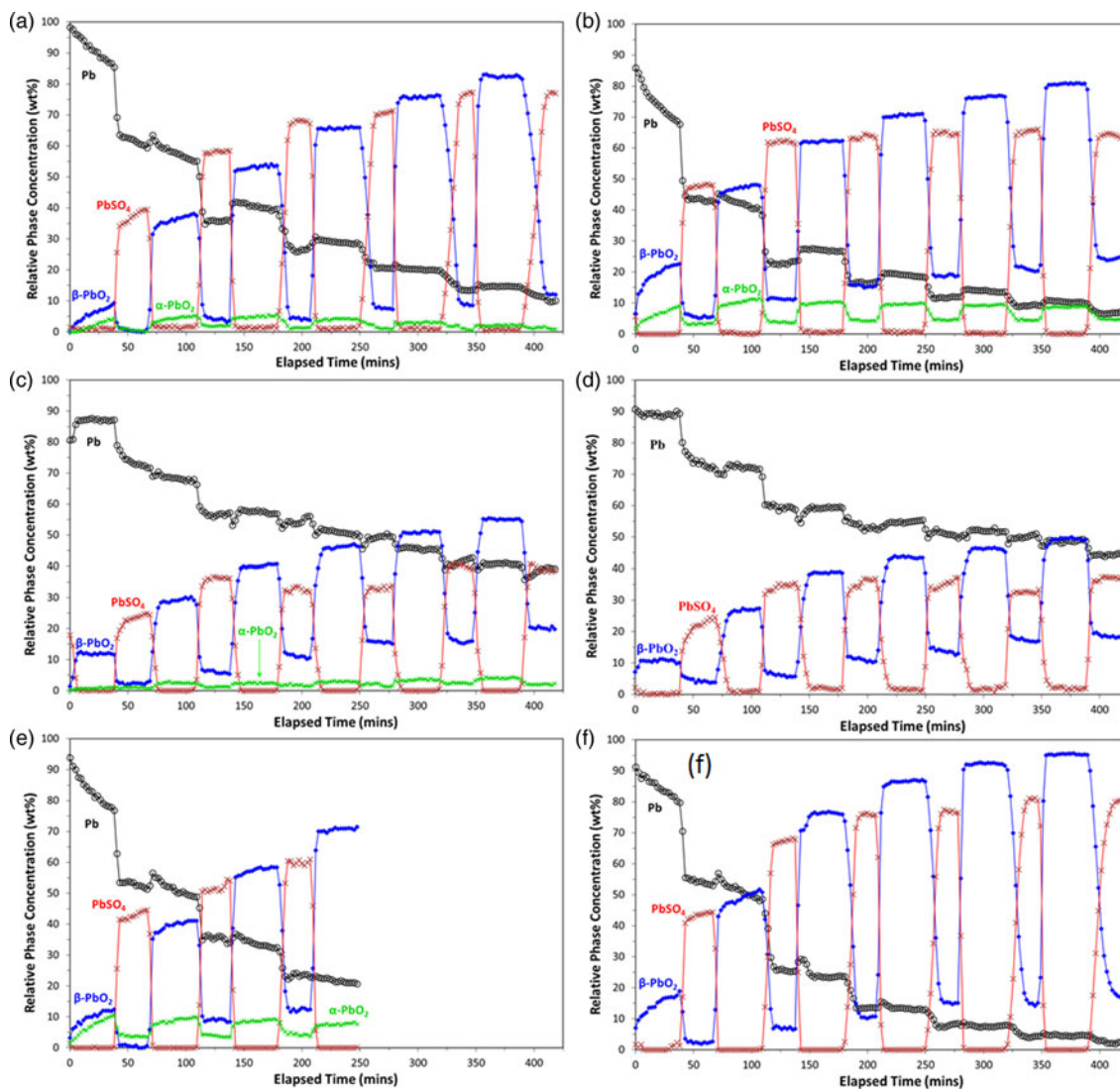


Figure 4. (Colour online) Results of Rietveld refinement-based quantitative phase analysis, showing the evolution in relative concentration of the alloy substrate and the  $\beta$ -PbO<sub>2</sub>,  $\alpha$ -PbO<sub>2</sub>, and PbSO<sub>4</sub> surface layers during the electrochemical tests for (a) Pb–0.08Ca–1.52Sn, (b) Pb–0.73Mg, (c) Pb–0.05Ag, (d) Pb–0.07Rh, (e) Pb–1.4Zn, and (f) pure Pb [reported by Clancy *et al.* (2015)]. In (e), at 248 min there was a loss of beam and so X-ray data were not collected beyond this point. The electrochemical cycling, however, was allowed to continue [Figure 1(d)].

is from the underlying substrate, the alloys with these higher phase concentrations (of  $\beta$ -PbO<sub>2</sub> and PbSO<sub>4</sub>) are likely to have thicker surface layers than Pb–Ag or Pb–Rh. It is suggested that Rh functions to lessen the rate of the PbO<sub>2</sub> to PbSO<sub>4</sub> transformation, resulting in a preference to retain a thinner, denser layer of  $\beta$ -PbO<sub>2</sub> on the substrate surface.

The evolution of the thickness of the PbO<sub>2</sub>/PbSO<sub>4</sub> surface layers formed on each alloy, calculated from the diffraction data using Eq. (1), is presented in Figure 5. The calculated surface layer thickness was greatest for the pure Pb anode. However, from electrochemical testing it was not the anode with the greatest surface layer thickness that had the poorest electrochemical performance, rather the Pb–Ca–Sn alloy (Figure 1). As such, the surface layer thickness appears not the prime factor in dictating anode performance, where a more detailed interpretation based on the results of the QPA reveals that poor electrochemical performance of the Pb–Ca–Sn alloy was governed chiefly by two factors. The first is that the relative amount of  $\beta$ -PbO<sub>2</sub> did not overtake that

of PbSO<sub>4</sub> until the fifth cycle – this occurred earlier for each of the other alloys (during the second cycle for Pb–Ag, Pb–Rh and Pb, during the third cycle for the Pb–Mg and Pb–Zn). As such the difference between the maximum  $\beta$ -PbO<sub>2</sub> and PbSO<sub>4</sub> concentrations during the sixth cycle is only 6 wt% for the Pb–Ca–Sn alloy. In contrast, the difference values for the Pb–Mg, Pb–Ag, Pb–Rh, and pure Pb anodes were 16, 14, 12, and 15 wt%, respectively. Secondly, the amount of retained  $\beta$ -PbO<sub>2</sub> during the OCP segments is lower for the Pb–Ca–Sn alloy than for the other anodes; 12 wt% during the sixth cycle, compared with 25, 20, 18, and 17 wt% for Pb–Mg, Pb–Ag, Pb–Rh, and pure Pb, respectively. It is, however, not completely clear at present if the stability of an anode alloy can be decided based on the dissolution of PbO<sub>2</sub> and subsequent formation of PbSO<sub>4</sub>. Other very important variables that can and will affect mass transport across the anodic layer that has formed are the associated porosity, conductivity, and texture limitations. Such factors require dedicated studies, however, the time-resolved

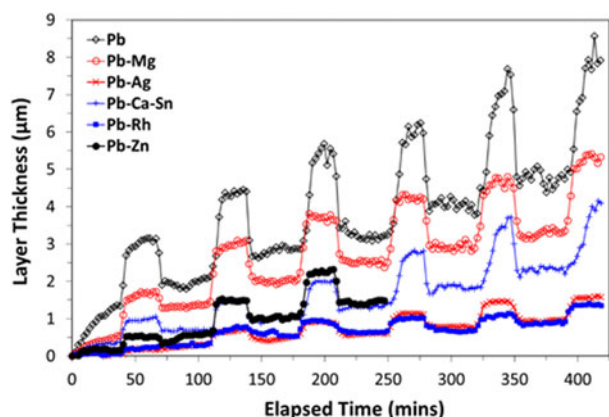


Figure 5. (Colour online) Calculated surface layer thickness as a function of time for each alloy.

measurements of relative phase fractions and surface layer thicknesses presented in this study provide significant new insights.

Further evidence of the layer thickness not being the sole determining factor in electrochemical behaviour is the comparison between the thickness curves for Pb–Mg and Pb–Zn in Figure 5, which are significantly different. Again, the key factor in determining electrochemical performance appears to be the similar proportions of the  $\text{PbO}_2$  and  $\text{PbSO}_4$  phases as cycling progressed [Figures 4(b) and 4(e)]. It is also noted that the model used to calculate the layer thickness [Eq. (1)] assumes that the density of the passivation layer is consistent across all of the samples. Variations in the density of this layer from sample to sample could affect the interpretation of the electrochemical performance. Further work is required to investigate the role of porosity within the passivation layers of these alloys. Based on the available data there is not considered to be sufficient evidence to determine whether or not the formation of  $\alpha\text{-PbO}_2$  is detrimental to the performance of an alloy material. Formation of the  $\alpha\text{-PbO}_2$  phase may be promoted by the presence of dopants with a tendency to form divalent cations, since the Pb–Mg and Pb–Zn alloys resulted in the formation of up to 11 wt% of this phase, with 5 wt% being the next highest amount observed (for the industry standard alloy which happens to contain Ca). Consequently, the influence of so-called “reactive elements” uniquely is also an area worthy of further pursuit.

#### IV. CONCLUSION

The effect of different alloying elements, Mg, Ag, Rh, and Zn, on the electrochemical performance of Pb-based anode alloys when exposed to alternating galvanostatic (operational) and open circuit (power interruption conditions) was assessed via *in situ* electrochemical S-XRD measurements. There was good correlation between the results, regarding the performance of the studied alloys, when assessed by both electrochemical and crystallographic methods. From an electrochemical perspective, Rh-additions produced an alloy with the most favourable electrochemical properties, although additions of Ag, Mg, and Zn also produced alloys with superior electrochemical performance compared with the industry standard Pb–Ca–Sn alloy. Such alloys were down selected

from a large number of alloys screened in preliminary work. The S-XRD measurements showed that a prevalence of  $\text{PbSO}_4$  relative to  $\text{PbO}_2$  was a detrimental factor with respect to electrochemical performance, in agreement with previous work in the field (Pavlov, 2011). The utility of such alloying in the industrial setting is however, beyond the scope of the present study, as factors such as cost and mechanical properties would need to be considered. Nevertheless, this present work is an important starting point for understanding the Pb-alloy surface film and the relationship between its composition and the attainment of desirable electrochemical performance. The present work also has relevance to electro-winning beyond that of Cu production, such as for the electro-winning of Zn, or in the context of lead-acid batteries. The level of research on Rh in particular is scarce (whereas Ag has been noted to offer energy savings in the solvent extraction industry), and considering the beneficial effects seen herein, alloying with Rh warrants further research from a metallurgical perspective and to elucidate the influence of Rh on the portfolio of Pb properties.

#### ACKNOWLEDGEMENTS

This research was undertaken on the powder diffraction beamline at the Australian Synchrotron, Victoria, Australia, under beamtime award AS141/M7391. The authors also acknowledge use of facilities within the Monash Centre for Electron Microscopy and financial support provided by the Australian Research Council’s Centres of Excellence funding scheme (CoE for Design in Light Metals) and the ARC Linkage Project Scheme. Thanks also to Nick Hardcastle of Consolidated Alloys for contributing materials to this project. The authors wish to thank Miao Chen (CSIRO Minerals Resources) for assistance with the electrochemical flow cell, Mark Gibson and Ian Madsen (CSIRO Manufacturing and Mineral Resources, respectively) for helpful discussions and Jean-Pierre Veder and Mikko Vepsäläinen (CSIRO Minerals Resources) for their assistance with the reference electrode preparation.

- Bruker (2014). TOPAS, version 5. Bruker AXS Inc., Madison, Wisconsin, USA.
- Butler, G. and Copp, J. L. (1956). “The thermal decomposition of lead dioxide in air,” *J. Chem. Soc.* 725–735.
- Camurri, C. P., López, M. J., Pagliero, A. N., and Vergara, F. G. (2001). “Deformations in lead–calcium–tin anodes for copper electro-winning,” *Mater. Charact.* 47, 105–109.
- Clancy, M., Styles, M. J., Bettles, C. J., Birbilis, N., Chen, M., Zhang, Y., Gu, Q., Kimpton, J. A., and Webster, N. A. S. (2015). “*In situ* synchrotron X-ray diffraction investigation of the evolution of a  $\text{PbO}_2/\text{PbSO}_4$  surface layer on a copper electro-winning Pb anode in a novel electrochemical flow cell,” *J. Synchrotron Radiat.* 22, 366–375.
- Cullity, B. D. (1978). *Elements of X-ray Diffraction*, 2nd ed. (Addison-Wesley, Reading), pp. 132–135.
- D’Antonio, P. and Santoro, A. (1980). “Powder neutron diffraction study of chemically prepared  $\beta$ -lead dioxide,” *Acta Crystallogr.* B36, 2394–2397.
- Goodwin, T. H. and Whetstone, J. (1947). “The crystal structure of ammonium nitrate III, and atomic scattering factors in ionic crystals,” *J. Chem. Soc.* 1455–1461.
- Hill, R. J. and Howard, C. J. (1987). “Quantitative phase analysis from neutron powder diffraction data using the Rietveld method,” *J. Appl. Crystallogr.* 20, 467–474.
- Pavlov, D. (2011). *Lead-Acid Batteries: Science and Technology* (Elsevier, Amsterdam).

- Pavlov, D. and Monahov, B. (1996). "Mechanism of the elementary electrochemical processes taking place during oxygen evolution on the lead dioxide electrode," *J. Electrochem. Soc.* **143**, 3616–3629.
- Rowles, M. R. (2010). "CONVAS2: a program for the merging of diffraction data," *Powder Diffr.* **25**, 297–301.
- Schlesinger, M., King, M., Sole, K., and Davenport, W. (2011). *Extractive Metallurgy of Copper*, 5th ed. (Elsevier, Amsterdam).
- Shannon, R. D. (1976). "Revised effective ionic radii and systematic studies of interatomic distances in halides and chalcogenides," *Acta Crystallogr.* **A32**, 751–767.
- Straumanis, M. E. (1949). "The precision determination of lattice constants by the powder and rotating crystal methods and applications," *J. Appl. Phys.*, **20**, 726–734.
- Wyckoff, R. W. G. (1963). *Crystal Structures* (John Wiley Interscience Publishers, New York), Vol. 1, pp. 239–444.